

# Experimental investigation of a flapping wing model

Tatjana Y. Hubel · Cameron Tropea

Received: 29 May 2008 / Revised: 24 September 2008 / Accepted: 18 November 2008 / Published online: 13 December 2008  
© Springer-Verlag 2008

**Abstract** The main objective of this research study was to investigate the aerodynamic forces of an avian flapping wing model system. The model size and the flow conditions were chosen to approximate the flight of a goose. Direct force measurements, using a three-component balance, and PIV flow field measurements parallel and perpendicular to the oncoming flow, were performed in a wind tunnel at Reynolds numbers between 28,000 and 141,000 (3–15 m/s), throughout a range of reduced frequencies between 0.04 and 0.20. The appropriateness of quasi-steady assumptions used to compare 2D, time-averaged particle image velocimetry (PIV) measurements in the wake with direct force measurements was evaluated. The vertical force coefficient for flapping wings was typically significantly higher than the maximum coefficient of the fixed wing, implying the influence of unsteady effects, such as delayed stall, even at low reduced frequencies. This puts the validity of the quasi-steady assumption into question. The (local) change in circulation over the wing beat cycle and the circulation distribution along the wingspan were obtained from the measurements in the tip and transverse vortex planes. Flow separation could be observed in the distribution of the circulation, and while the circulation derived from the wake measurements failed to agree exactly with the absolute value of the circulation, the change in circulation over the wing beat cycle was in excellent agreement for low and moderate reduced frequencies. The comparison between the PIV measurements in the two perpendicular planes and the direct force balance measurements, show that within certain limitations the

wake visualization is a powerful tool to gain insight into force generation and the flow behavior on flapping wings over the wing beat cycle.

## 1 Introduction

Recent interest in the development of micro air vehicles (MAVs) has brought attention to the fundamental aerodynamics of flapping flight (Mueller 2001). In order to gain a better understanding of the flow behavior on moving wings at low Reynolds numbers, aerodynamics, kinematics, morphology and energy consumption of animal flight have been recently studied with renewed interest (Dickinson et al. 1999; Ellington 1999; Rayner and Gordon 1998; Sane 2003; Spedding et al. 2003b). In spite of the increasing research in flapping flight over the last decade, many questions are still unresolved in order for flapping flight to be used in engineering applications. Not only is the unsteady aerodynamic research field at these Reynolds numbers and reduced frequencies comparatively new, but also the flow behavior in the MAV Reynolds number range (<100,000) is quite distinct from the performance at higher Reynolds numbers more characteristic of aircraft.

The challenge to better understand the aerodynamic and kinematic aspects of flapping flight and the correlation between them is accompanied by additional laboratory challenges posed by moving test objects. Direct force measurements on swimming and flying animals are difficult to perform and analyze, especially in untethered conditions. A small number of successful measurements on tethered insects such as locusts (Cloupeau et al. 1979; Wilkin 1990; Zarnack 1969), moths (Bomphrey et al. 2005; Wilkin 1991; Wilkin and Williams 1993), fruit flies

---

T. Y. Hubel (✉) · C. Tropea  
Fachgebiet Strömungslehre und Aerodynamik,  
Technische Universität Darmstadt, Darmstadt, Germany  
e-mail: tatjana\_hubel@brown.edu

(Dickinson and Gotz 1996) and dragonflies (Thomas et al. 2004) have been conducted. Vertebrates generally refuse to fly or swim under tethered conditions; therefore, direct force and drag measurements are limited to dead animals and body parts (Maybury and Rayner 2001, Webb 1975). Similarly, pressure measurements on animals are difficult; hence even fewer examples of successful force measurements have been collected (Usherwood et al. 2003, 2005).

Contrary to former visualization tools such as smoke that provided only qualitative (Thomas et al. 2004; Willmott et al. 1997) or helium bubbles with limited quantitative insight into the flow behavior (Spedding 1986, 1987a, b; Spedding et al. 1984), current optical measurement techniques, such as particle image velocimetry (PIV), are often used for quantitative investigations of the wake flow field in terms of the instantaneous velocity and vorticity fields (Drucker and Lauder 1999; Spedding et al. 2003a, b; Warrick et al. 2005).

This present study was conducted by applying Helmholtz's vortex laws, to estimate the generated forces from a 2-D plane perpendicular to the flow stream. Accordingly, the circulation in a closed vortex ring is equal throughout. Therefore the tip-vortex circulation of a single wing should be equal to that of the bound vortex circulation from which the lift is obtained by applying the Kutta-Joukowski theorem. While the measurements in the tip vortex plane contain the information about the total circulation of the bound vortex and the change in circulation over the wing beat cycle, measurements parallel to the flow in the transverse vortex plane contain information about the local change in circulation across the span.

The comparison with direct force measurements was used to assess how suitable simple 2D PIV measurements

are to estimate the time-resolved generated lift forces on the wing using the Kutta-Joukowski theorem.

## 2 Methods and materials

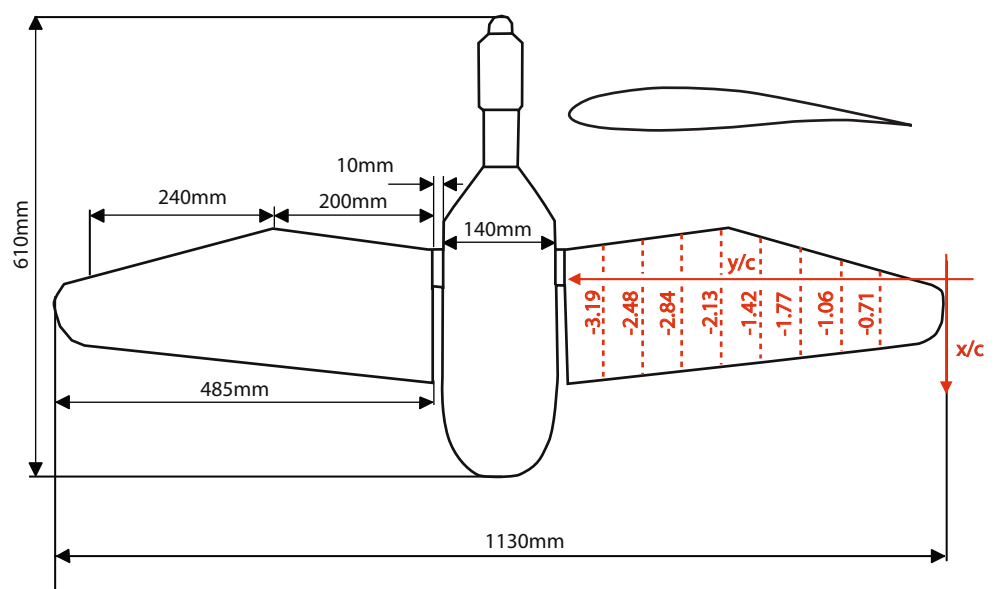
The flapping-wing model was investigated in the low-speed wind tunnel (test section 2.90 width  $\times$  2.20 height  $\times$  4.90 m length, turbulence level  $<$  1%) at the Technische Universität Darmstadt. Flow visualization using PIV and direct force measurements using a three-component balance were performed on fixed wings as well as flapping wings. Vertical force, horizontal force, and pitching moment coefficients were calculated from the balance, after taking into consideration the inertial forces and added mass effect in the case of the flapping wings. For the comparison between fixed wing and flapping wing measurements the effective angle of attack was calculated at mid wing-span.

Vorticity, circulation, the distribution of the circulation, and the lift coefficient were calculated based on visualization perpendicular to the flow stream. Due to the distance separating the measurement plane in the wake from the wing itself (distance 2.2 chord lengths ( $c$ )), a time lag between wing position and wake characteristics can be expected. This was compensated by delaying the comparison times by the separation distance divided by the free-stream velocity (Hubel 2006).

### 2.1 Flapping wing model

The model was about the size of a goose (wingspan 1.13 m; average wing chord ( $c$ ) 0.141 m; Fig. 1). The

**Fig. 1** Flapping wing model and wing profile



wings were made of fiberglass and epoxy resin. The model was powered by a direct current motor with a maximum flapping frequency of 2.2 Hz, controlled by a 4-Q-EC Servoamplifier. The body covered the driving mechanics and the three-component balance inside the model.

The static angle of attack ( $\alpha_0$ ) was adjusted at the shoulder joint. The flapping motion was asymmetrical, where the typical deflection below horizontal was  $17^\circ$  and above horizontal  $27^\circ$ . Depending on wind speed, the Reynolds number was between 28,000 and 141,000 (3–15 m/s) and the reduced frequency between 0.04 and 0.20, where the reduced frequency was defined as  $k = (\pi fc)/U_\infty$  ( $f$  is wingbeat frequency,  $U_\infty$  the free-stream velocity, and  $c$  the average wing chord).  $Re$  and  $k$  were therefore typical of bird and large insect flight; however, similar to animal flight not independent from each other. The variation in Reynolds number and reduced frequency was accomplished by changes in wind speed, so that the highest reduced frequencies were accompanied by the lowest Reynolds numbers. Due to the large discrepancy between the wing profiles of resting versus flying birds, a realistic goose-like wing profile under loading was not available and a profile comparable to the proximal wing section of a gliding bird (cambered profile with rounded leading edge); a Wortmann Fx-60-126 was used across the entire wingspan.

## 2.2 Direct force measurements

Vertical force, horizontal force, and pitching moment were recorded as a function of time using an internal three-component balance, which was located between the model and the holder. The three-component balance was built of 4 force transducers: three vertical and one horizontal, mounted between two plates. Forces and moment were obtained by using the calibration matrix generated under single and combination loads. The measurement range ( $r$ ) and precision ( $p$ ) of the balance was as follows: vertical force ( $r = \pm 115$  N,  $p = 0.02\%$ ), horizontal force ( $r = \pm 40.5$  N,  $p = 0.6\%$ ) and pitching moment ( $r = \pm 5.3$  Nm,  $p = 1.5\%$ ).

Measurements under steady flow conditions with horizontally fixed wings, as well as under unsteady conditions with flapping wings, were performed. The measurement rate was between 300 and 600 Hz, depending on the flapping frequency. Up and downstroke were separated and the forces were interpolated over the amplitude angle and averaged over 10–15 wing beat cycles. A Butterworth low-pass filter was used to eliminate noise, such as the natural frequency of the wings (22 Hz) and balance (11 Hz), in the force measurements above 10 Hz.

Vertical-, horizontal and pitching coefficients were calculated from the averaged forces and moment in the

following manner and referenced to a constant wing area, where the body area between the wings was included.

Vertical force coefficient ( $C_z$ )

$$C_z = \frac{2F_z}{\rho U_\infty^2 A} \quad (1)$$

Horizontal force coefficient ( $C_x$ )

$$C_x = \frac{2F_x}{\rho U_\infty^2 A} \quad (2)$$

Pitching moment coefficient ( $C_m$ )

$$C_m = \frac{2M_y}{\rho U_\infty^2 A c} \quad (3)$$

where  $F_z$  is the vertical force,  $F_x$  is the horizontal force,  $M_y$  is the pitching moment,  $U_\infty$  the free-stream velocity,  $A$  the wing area,  $\rho$  the density, and  $c$  the average wing chord.

The average standard deviation for balance measurements over a wing beat cycle was typically in the range of 0.004–0.009 for the vertical force coefficient and in a range of 0.0007–0.003 for the horizontal force coefficient. The magnitude depended on the reduced frequency, increasing slightly with decreasing  $Re$  and higher flapping frequency, but exhibiting no correlation for different angles of attacks.

### 2.2.1 Fixed wing

In case of the measurements under steady flow conditions, the wings were fixed in the horizontal position and the static angle of attack was adjusted at the shoulder joint. Measurements at different static angles of attack ( $\alpha_0 = 0^\circ$ – $12^\circ$ ) and Reynolds numbers ( $U_\infty = 28,000, 56,000, 85,000, 113,000, 141,000$ ) were performed. The lift coefficient versus angle of attack of a 2-D Wortmann Fx-60-126 Profile at  $Re = 100,000$ , published in (Althaus 1981) was taken as a reference. The 2D coefficients were transferred into 3D wing coefficients by using Prandtl's lifting line theory:

$$C_{L3D} = C_{L2D} \left( \frac{1}{1 + a_0/\pi e AR} \right) \quad \text{with} \quad a_0 = \frac{\Delta C_{L2D}}{\Delta \alpha^\circ} \frac{180}{\pi} \quad (4)$$

where  $AR$  is the aspect ratio of the wing and  $e$  the Oswald efficiency factor that was assumed to be 1, although the lift distribution on the model was presumably not perfectly elliptical.

### 2.2.2 Dynamic forces and added mass effects on flapping wings

Contrary to measurements under steady conditions, the results of force measurements on flapping wings comprise

not only the aerodynamic forces, but are a combination of the aerodynamic forces, dynamic forces and added mass effect. Therefore, in order to eliminate the contributions of the dynamics forces and added mass, each test case was performed twice, once with and once without wind. The test results without wind were then subtracted from the test results with wind. This was performed with the assumption that the inertial forces generated under wind load conditions were the same as when testing without wind. To determine the added mass effect additional measurements were performed using appropriately weighted tars in place of the wings. Here the assumption is made that these tars provide the same inertial forces as when testing with the actual wings themselves, the difference between the measurements with wings and rods (both performed without wind) being taken to represent the added mass force.

As a comparison to the measurements, the added mass force was calculated for a sinusoidal movement with a flapping frequency of 2 Hz. The centre of the added mass was assumed to be located at half of the wing chord and according to Walker 2002, the added mass force  $F_{add}$  can be calculated using the following equation:

$$F_{add}(r, t) = \frac{\pi}{4} \rho c^2(r) \dot{v}_n(r, t) \beta_n dR \tag{5}$$

where  $R$  is the wingspan,  $r$  the position along the wingspan and  $\beta_n$  the added mass coefficient ( $\beta_n = 1$ ).

For a flapping wing without a pitching movement the acceleration normal to the surface  $\dot{v}_n$  is:

$$\dot{v}_n(r, t) = r \ddot{\theta}(t) \tag{6}$$

$$\theta(t) = \theta_1 \sin(\omega t) \tag{7}$$

$$\dot{\theta}(t) = \omega \theta_1 \cos(\omega t) \tag{8}$$

$$\ddot{\theta}(t) = -\omega^2 \theta_1 \sin(\omega t) \tag{9}$$

where  $\theta$  is the amplitude angle,  $\theta_1$  the maximum amplitude of  $22^\circ$  (neglecting the difference in deflection below and above horizontal) and  $\omega$  the angular velocity.

### 2.2.3 Flapping wings

In order to obtain the difference between measurements under static conditions and measurements with flapping wings the results were shown as force coefficient versus angle of attack. For flapping wings the effective flow direction is a result of the horizontal free-stream velocity  $U_\infty$  and the vertical velocity component ( $v_z$ ) caused by the flapping movement. For an infinite span 2D airfoil with only a plunge motion the effective angle of attack ( $\alpha_{eff}$ ) is:

$$\alpha_{eff}(t) = \alpha_0 + \arctan \frac{v_z(t)}{U_\infty} \tag{10}$$

where  $\alpha_0$  is the angle of attack under static conditions. However, because the wings pivot about the shoulder joint the local velocity changes along the span. If the wing bending is negligible there is a linear increase of the vertical velocity towards the wing tip. The increasing influence of the vertical velocity towards the tip results in an increasing effective angle of attack as shown in Fig. 2.

The effective angle of attack of the flapping wing was calculated at the mid-span position of the wing. The vertical velocity was calculated in following manner:

$$v_z(t) = \frac{h(t_2) - h(t_1)}{t_2 - t_1} \tag{11}$$

where  $t$  is time and  $h$  is the local horizontal position of the wing:

$$h(t) = r \sin \theta(t) \tag{12}$$

$\theta$  is the amplitude angle and  $r$  the distance from the wing root.

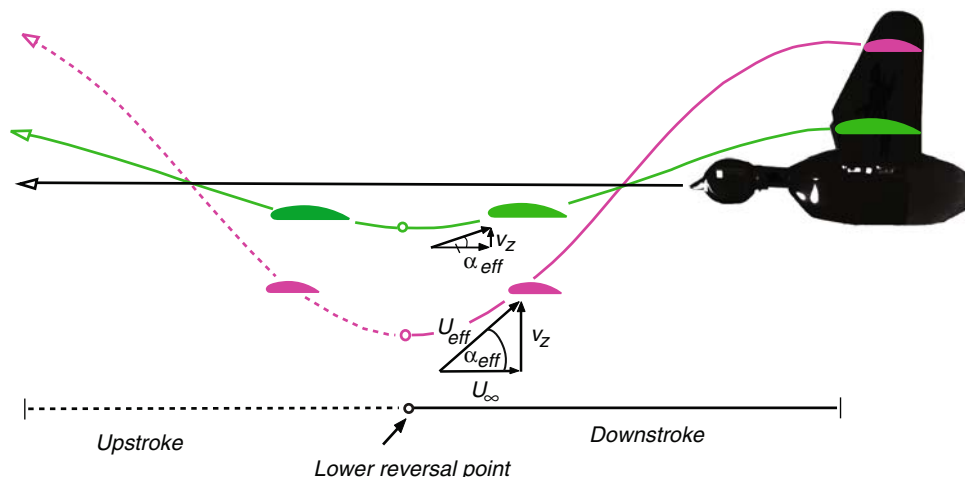


**Fig. 2** Path of the proximal and distal wing areas, showing the increasing influence of the vertical velocity towards the wing tip

### 2.3 Flow visualization perpendicular to the flow stream (tip-vortex plane)

Particle image velocimetry (PIV) was used to capture the instantaneous velocity-field in the plane perpendicular to the flow stream. The observation area was positioned 2.2 wing chords downstream of the trailing edge and was patched together using multiple camera positions due to the large flapping amplitude. The area was illuminated with a 200 mJ Nd:YAG double-pulse laser (New Wave Gemini 200), producing a pulse width of 10 ns and a variable duration between pulses. Images were taken with two CCD cameras (PCO SensiCam, 1,024 × 1,280 Pixels) mounted on a traversing system at the end of the test section. The vector field was calculated by using the adaptive correlation function in the standard two-dimensional PIV software system from Dantec Dynamics (Flow Manager®). The Interrogation area was 32 × 32 pixels with a 50% overlap, and a validation area that included 3 × 3 pixels. All further processing was carried out in Matlab® (MathWorks, Inc., Natick MA, USA). The first image in the wing-beat cycle was triggered via a rotational potentiometer in the model, while all subsequent images were triggered via pre-set time stepping. Because of the low pulse frequency of the laser (10 Hz), the wing-beat cycle was reconstructed from measurements over many wing beat cycles (25–50) to obtain sufficient resolution of the wing beat cycle. For each wing-beat cycle, 50–70 positions were sampled, depending on the wing-beat frequency. For the static wing measurements, in which the wings were fixed in the horizontal position, 500 image pairs were sampled and averaged. The standard deviation depended on the measurement position along the span, showing significant higher values for the area close to the body and increased with increasing reduced frequency.

The vorticity ( $\omega$ ) in the observation area was calculated from the vector field in the following manner:

$$\begin{aligned} \omega_x &= \frac{\partial w}{\partial y} - \frac{\partial v}{\partial z} \quad (\text{streamwise}) \\ \omega_y &= \frac{\partial u}{\partial z} - \frac{\partial w}{\partial x} \quad (\text{transverse}) \end{aligned} \tag{13}$$

Subsequently, the circulation ( $\Gamma$ ) over the measurement plane was calculated through integration of the vorticity over the observation area in the following manner:

$$\Gamma = \iint_A \omega dA \tag{14}$$

The circulation measured in the longitudinal tip vortices can be related to the lift ( $L$ ) production via the Kutta-Joukowski relation:

$$L = \rho U_\infty \int_{-b/2}^{b/2} \Gamma(y) dy \tag{15}$$

Subsequently the lift coefficient ( $C_L$ ) is given by:

$$C_L = \frac{2L}{\rho U_\infty^2 A} = \frac{2}{U_\infty A} \int_{-b/2}^{b/2} \Gamma(y) dy \tag{16}$$

In order to calculate the total circulation on the wings, the vorticity was integrated over the entire observation area. However, information about the distribution of the circulation can be obtained by separating the observation area in small strips (Fig. 3). The circulation of each strip was calculated in order to obtain the variation in circulation in spanwise direction.

The circulation was calculated from the vorticity field by integration over the strip area ( $A_i$ ):

$$\Delta\Gamma_i = \iint_{A_i} \omega_{x,i} dA_i \tag{17}$$

Subsequently, the change in circulation was normalized with the free-stream velocity ( $U_\infty$ ) and the average wing chord ( $c$ ):

$$\Delta\gamma_i = \frac{\Delta\Gamma_i}{U_\infty c} \tag{18}$$

In order to obtain the distribution of the circulation rather than the local circulation itself, the change in circulation was summed over the wingspan, in the following manner:

$$\gamma_i = \sum_{j=1}^i \Delta\gamma_j \tag{19}$$

The distribution was compared to analytic calculations based on Multhopp’s method of solving Prandtl’s lifting line theory by using linear equations at specific locations along the span (Multhopp 1938). Multhopp’s method is a quasi-steady estimation, which includes neither boundary effects, unsteady effects, body wing interactions, nor Reynolds number influence.

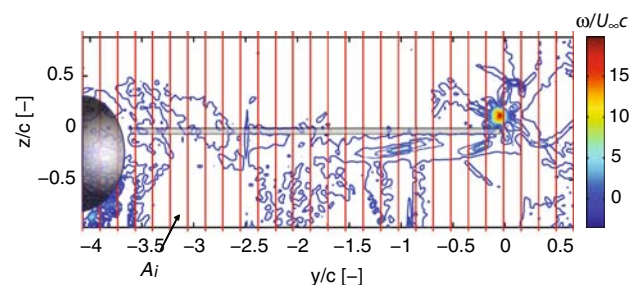


**Fig. 3** Contours of normalized vorticity illustrated over partitioned observation areas ( $A_i$ ) behind the wing (Trefftz plane)

#### 2.4 Flow visualization parallel to the flow stream (transverse vortex plane)

In order to obtain the change in circulation in the transverse vortex plane, PIV measurements in the vertical plane parallel to the flow direction were performed at several wingspan positions (Fig. 1).

The change of circulation in the spanwise direction was obtained by calculating the vorticity contained in the start/stop vortices leaving the trailing edge. The change of bound circulation on the wing in a time interval  $\Delta t = t_{i+1} - t_i$  can be calculated in the following manner:

$$\Delta\Gamma = \oint_{C_{i+1}} \vec{v} d\vec{l} = \iint_{A_{i+1}} \omega_y dA \quad (20)$$

where the contour  $C_{i+1}$  or area  $A_{i+1}$  are given by the material lines of the fluid elements starting from a fixed line located immediately downstream of the trailing edge.

This method requires in theory the time-resolved acquisition of the wake-velocity field and a corresponding Lagrangian particle tracking but was simplified by using the streamwise velocity component to define the downstream contour of the area, i.e.

$$d(z) = \frac{[u_i(z) + u_{i+1}(z)]}{2} \Delta t \quad (21)$$

where  $u_i$  and  $u_{i+1}$  are the velocities at the upstream and downstream end of the integration area and  $\Delta t = T/N$ , with  $N$  number of images over one wing-beat period  $T$ .

#### 2.5 Comparison of PIV results (Tip and transverse vortex plane)

To compare the results from the tip-vortex plane and the transverse vortex plane, the change of circulation in the observation area perpendicular to the flow stream was calculated close to the same spanwise location where the transverse vortices were visualized. However, while the transverse vortex plane showed the vortex generation in a narrow plane, limited by the laser-light sheet thickness to approximately 3 mm, observations in the tip vortex plane require a certain size for the integration area (see  $A_i$  in Fig. 3) and consider the vortex development over a larger area along the span ( $y/c = 0.22$ ).

#### 2.6 Comparison of balance and PIV results (Tip vortex plane)

The comparison between PIV and balance results was complicated due to the fact that vertical and horizontal forces measured by the balance equal lift and drag only under horizontal fixed wing conditions. On flapping wings

the incident flow direction changes constantly due to the changing influence of the vertical velocity along the span and during the wing beat cycle, leading to a constant change in lift direction. A direct comparison between balance results ( $C_z$ ) and PIV results ( $C_L$ ), would require a transformation of either  $C_z$  or  $C_L$ , which requires detailed information about the lift distribution on the wing over the whole wing beat cycle. Although the tip vortex measurements provided a good insight into this distribution (as can be seen later) it did not provide the information on the wing itself. Direct comparisons between the results of the two investigation methods were therefore not strictly possible, but assuming that the lift force dominated the vertical force component, the comparison of the vertical component value to the wake lift measurement was felt to be justified.

### 3 Results

#### 3.1 Direct force measurements

##### 3.1.1 Fixed wing

The comparison of the fixed wing measurements with the calculated 3D results based on (Althaus 1981) exhibits good agreement (Fig. 4a).

The lift coefficients at higher Reynolds numbers match well the literature based 3D calculation in the linear range of the wing. At higher angles of attack the stall induced decrease of the lift coefficient was slightly smoother in the case of the model. The differences were likely caused by the interference between body and wings of the model. The lift coefficients clearly showed a Reynolds number dependency: the results of measurements at  $Re = 28,000$ , were drastically lower. At such low Reynolds numbers there were apparently large areas of laminar flow while at higher Reynolds numbers the flow was predominantly turbulent. The dependence of the flow condition on the Reynolds number can also be seen in the drag polars (Fig. 4b) and the pitching coefficient in (Fig. 4c).

##### 3.1.2 Dynamic forces and added mass effects on flapping wings

Following the procedure outlined above, example measurements are presented to indicate the magnitude of the corrections for inertial forces and added mass effects. In Fig. 5a and b the total measured force and the force measured without wind are shown. The subtraction of the results measured without wind reveals that the vertical force generation over the upstroke was considerably lower than during the downstroke (Fig. 5c). Furthermore, the results of the vertical force generated without wind showed

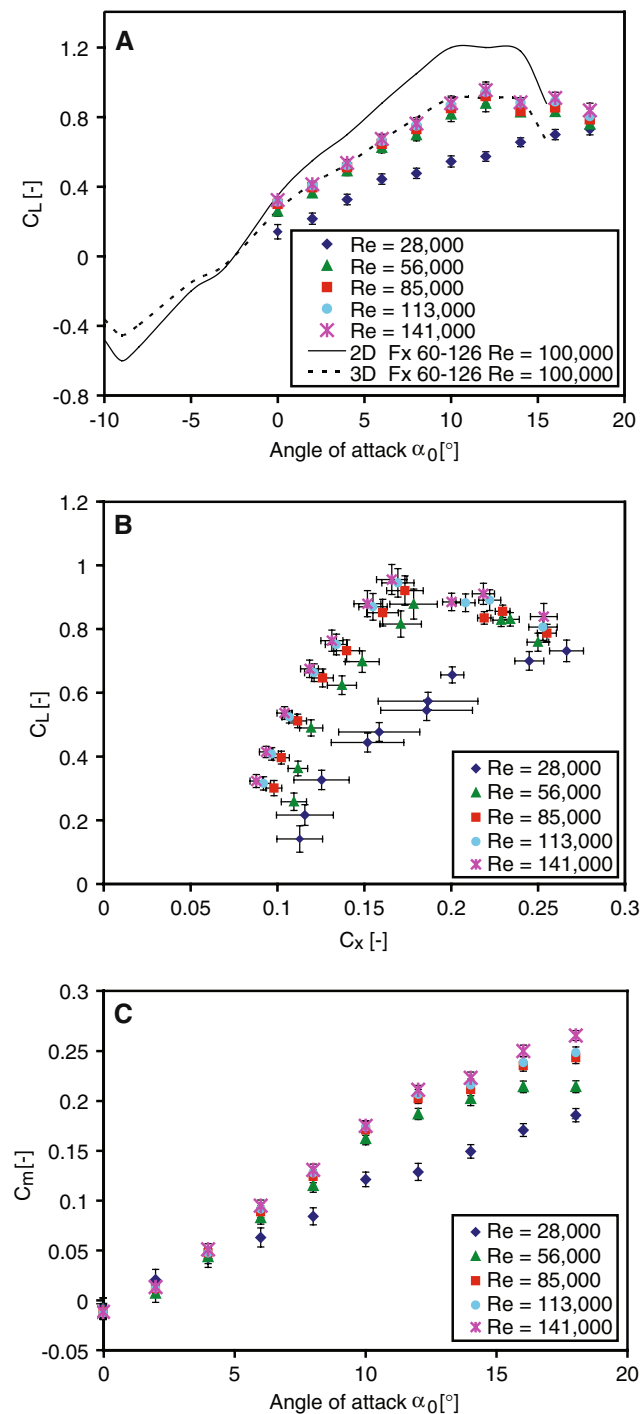


**Fig. 4** a Lift coefficient ( $C_L$ ) versus angle of attack ( $\alpha_0$ ) of the fixed wings at different Reynolds numbers compared to the lift performance of a Wortmann Fx 60-126 Profile (from Althaus 1981). The 3D results are derived from the 2D data using lifting line theory. b Lift coefficient ( $C_L$ ) versus drag coefficient ( $C_D$ ) of the fixed wings at different Reynolds numbers. c Pitching moment coefficient ( $C_m$ ) versus angle of attack ( $\alpha_0$ ) of the fixed wings at different Reynolds numbers

that the inertial forces and added mass effects combined were of the same magnitude as the aerodynamic forces. The inertial forces were provided by the replacement of the

wings with rods (Fig. 5d). The added mass was obtained by subtracting these results from the results from measurements with wings but without wind. According to these measurements the added mass force was less than 10% of the aerodynamic force in this particular example. Added mass forces are highly dependent on the acceleration of the wings, which do not always perform a sinusoidal movement, but recent studies in bird and insect flight show that values around 10% are very reasonable (Hedrick et al. 2004; Dickson and Dickinson 2004).

The comparison between the result of the added mass calculation and the measured added mass effect showed values of the same order of magnitude (Fig. 6). The effect of the non-sinusoidal movement was clearly visible in the phase difference to the sinusoidal results and the strong acceleration at the lower reversal point was reflected in the quickly increasing added mass force during this wing beat phase.

### 3.1.3 Aerodynamic forces and moments on flapping wings

The force generation on the wings changes over the wing beat cycle as well as with the spanwise position. While the balance results do not give insight into the events along the wingspan the change of the total force can be illustrated in relation to the phase of the wing beat cycle, indicated by the amplitude angle of the wing. The development of  $C_z$  during the wing beat cycle is correlated with the reduced frequencies, whereas the variation of  $k$  was either obtained through a change in the free-stream velocity (Fig. 7a) or the flapping frequency.

$C_z$  during the downstroke was considerably higher than during the upstroke for all  $k$ . The flow conditions close to the reversal points were the most similar to steady flow conditions due to the minimum of vertical velocity. Nevertheless there was still a considerable influence of the aerodynamic phase lag, causing slightly different  $C_z$  values for the upper and lower reversal points. The  $Re$  dependency, known from the fixed-wing measurements, can also be seen at the reversal points, especially for the results at  $Re = 28,000$ , which are significantly lower than at higher  $Re$ .

For  $k < 0.14$  a positive vertical force ( $C_z$ ) was generated during both the downstroke and upstroke. However, for increasing  $k$  the difference of  $C_z$  during the downstroke and upstroke became larger to the point of generating negative  $C_z$  values during the middle parts of the upstroke. The increasing contribution of the vertical velocity component to the effective angle of attack at high  $k$  contained also the risk of flow separation. At  $k = 0.20$  the effective angle of attack exceeded  $48^\circ$  at the wing tip (without consideration of the induced angle of attack). In this case, flow separation occurred on distal wing areas, which is indicated by

**Fig. 5** Vertical force ( $F_z$ ) versus amplitude angle ( $\theta$ ) for flapping wings at  $\alpha_0 = 0^\circ$  and  $f = 2$  Hz including the standard deviation (displayed only for every third value). **a** Total vertical force at  $U_\infty = 9$  m/s. **b** Vertical force ( $F_z$ ) representing the inertial and added mass effects at  $U_\infty = 0$  m/s. **c** Vertical aerodynamic force after the subtraction of the inertial and added mass effects at  $U_\infty = 9$  m/s. **d** Measurement of inertial effects using rods instead of wings at  $U_\infty = 0$  m/s

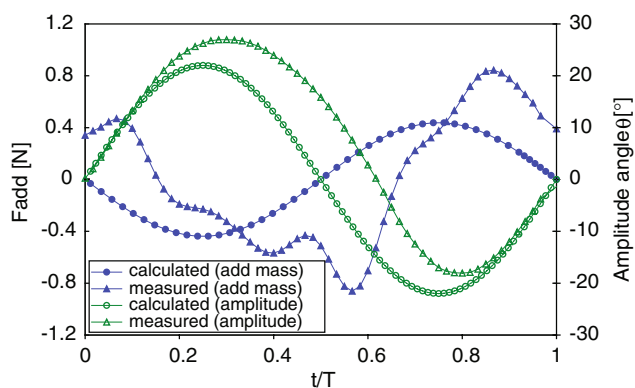
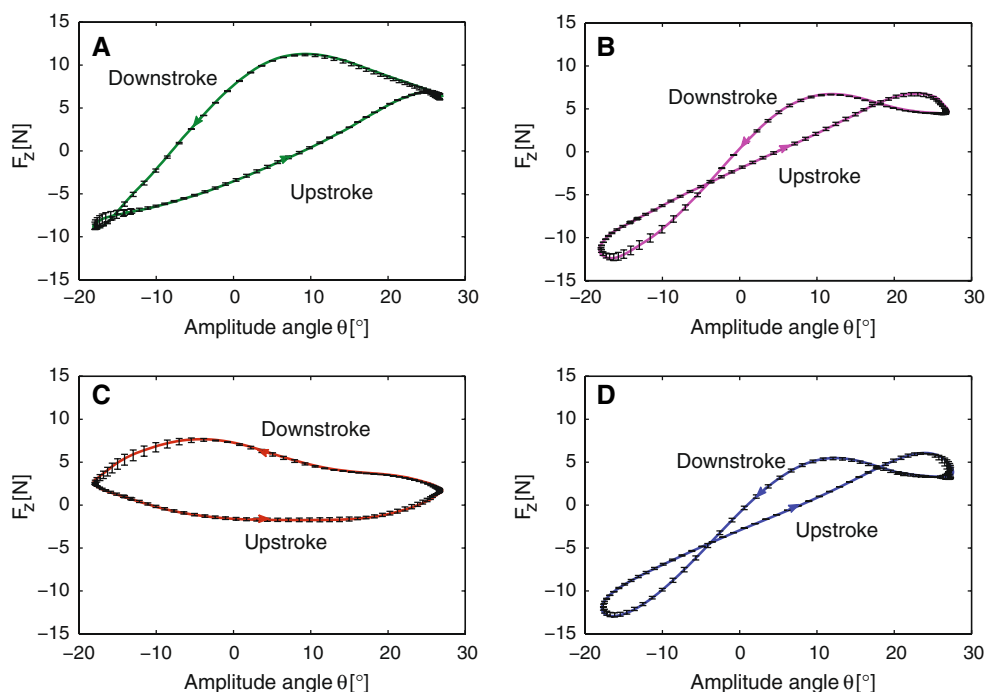


**Fig. 6** Comparison of the measured added mass force ( $F_{\text{add}}$ ) and calculated added mass force (based on Walker 2002) at  $\alpha_0 = 0^\circ$  and  $f = 2$  Hz

reaching  $C_{z_{\text{max}}}$  (maximum lift) before reaching the maximum effective angle of attack, while otherwise at low  $k$   $C_{z_{\text{max}}}$  occurred after reaching the maximum angle of attack due to the aerodynamic phase lag.

Not only  $C_z$  but also the  $C_x$  generation changed during the wing beat cycle (Fig. 7b). The deviations of drag generation at the reversal points from static conditions was indicated by lower and higher  $C_x$  values in relation to the  $C_x$  values at the reversal points. There was a considerable decrease in the  $C_x$  generation during the downstroke at all  $k$ . However, while the  $C_x$  generation during the upstroke was higher than at the reversal points for low  $k$ , there was an additional thrust generation during the upstroke at  $k = 0.07$  due to the negative  $C_z$  generation at distal positions of the wings.

The static angle of attack was not only changed for the fixed wings but also varied in the case of the flapping wings, increasing the  $\alpha_{\text{eff}}$  over the wing beat cycle at given  $k$ .  $C_z$  values increased with increasing  $\alpha_0$  during the downstroke as well as during the upstroke. While the change of  $C_z$  over the wing beat cycle for low  $\alpha_0$  was very similar, and the increasing  $\alpha_0$  acted comparable to an offset (Fig. 8a), effects such as flow separation changed the shape of the curve at higher  $\alpha_0$  especially at high  $k$  (Fig. 8b).

### 3.1.4 Comparison between fixed and flapping wings

A direct comparison between the results of the flapping wings and static measurements was obtained by showing  $C_z$  versus the (effective) angle of attack, which also allowed new insights into the  $C_z$  development over the wing beat cycle. At low  $k$  and relatively high Reynolds number ( $k = 0.04$ ,  $Re = 141,000$ ), through which the flow conditions tend to be more quasi-steady, the  $C_z$  values at the reversal points were close to the results of the static measurements (Fig. 9a). However, the maximum  $C_z$  value of the flapping wings at  $\alpha_0 > 6^\circ$  was significantly higher as  $C_{z_{\text{crit}}}$  for fixed wings. Therefore the  $C_z$  enhancement was considered as an unsteady effect, which occurs even at relatively low  $k$ . The influence of this unsteady effect increased at higher  $k$ , as can be seen in Fig. 9b. In addition, the consequence of flow separation is also clearly recognizable in the rapid decrease of the  $C_z$  values around the maximum effective angles of attack.



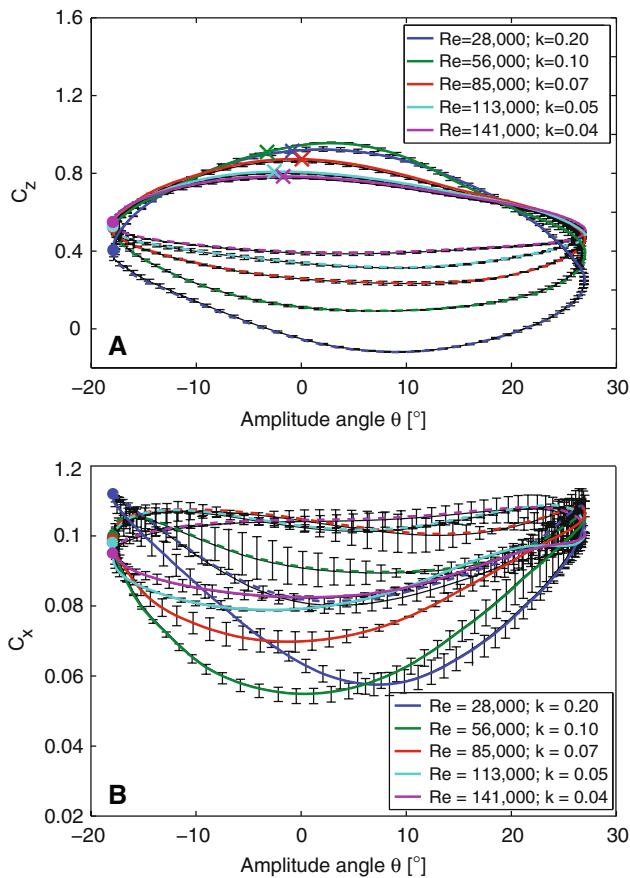


**Fig. 7** **a** Vertical force coefficient ( $C_z$ ) and **b** horizontal force coefficient ( $C_x$ ) versus amplitude angle ( $\theta$ ) at different Reynolds numbers ( $Re$ ) for  $\alpha_0 = 4^\circ$  and  $f = 1.28$  Hz, including the standard deviation (displayed only for every third value). Upstroke (*dashed line*); downstroke (*continuous line*); lower reversal point (*circle*); maximum effective angle of attack (*cross*)

But not only  $C_z$  values can yield insight into the flow conditions on the wings. Thrust generation and flow separation are visible in the comparison between the  $C_x$  values under fixed-wing conditions and those generated by flapping wings. At relative low reduced frequencies the  $C_x$  values increase during the upstroke but decrease remarkably during the downstroke because of the high thrust generation (Fig. 9c). The non-linear increase in drag generation increased the inclination of the curves and the aerodynamic phase shift with increasing  $\alpha_0$ .

At higher  $k$  flow separation effects have dramatic influences at higher  $\alpha_0$  (Fig. 9d). There was a sudden increase in the  $C_x$  values at high  $\alpha_{eff}$  during the downstroke, due to the flow separation over large parts of the wings. The dominant stall influence was also recognizable in the  $C_m$  values. While the curve shape at low  $\alpha_0$  was nearly linear the flow separation caused a significant bend in the curve progression (Fig. 9e).

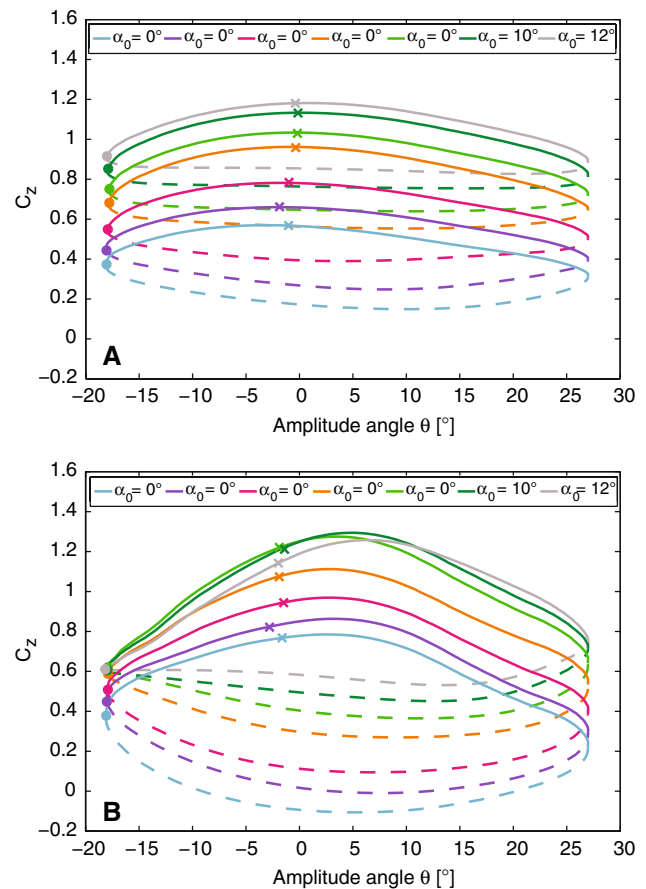


**Fig. 8** **a** Vertical force coefficient ( $C_z$ ) versus amplitude ( $\theta$ ) at different  $\alpha_0$  for  $k = 0.04$  ( $f = 1.28$  Hz,  $Re = 141,000$ ). **b** Vertical force coefficient ( $C_z$ ) versus amplitude ( $\theta$ ) at different  $\alpha_0$  for  $k = 0.10$  ( $f = 1.28$  Hz,  $Re = 56,000$ ). Upstroke (*dashed line*); downstroke (*continuous line*); lower reversal point (*circle*); maximum effective angle of attack (*cross*)

### 3.2 Flow visualization perpendicular to the flow stream

The circulation (Fig. 10a) and the distribution of the circulation (Fig. 10b) behind fixed wings showed that the roll-up process behind the wing was not completed 2.2c downstream of the wing. The circulation was highest close to the wing tip region where the tip-vortex was located. In addition, there was a significant amount of the circulation distributed along the span. There was a considerable amount of negative circulation near the body, where the standard deviation was significantly higher than in other parts of the observation area.

The comparison with simple quasi-steady calculations according to Multhopp (Fig. 11) showed that the values based on the Multhopp calculation at high  $Re$  are of the same magnitude as the PIV based calculations and take a similar course apart from the area near the body. The change in the distribution of the circulation over the wing beat cycle was clearly visible at all reduced frequencies

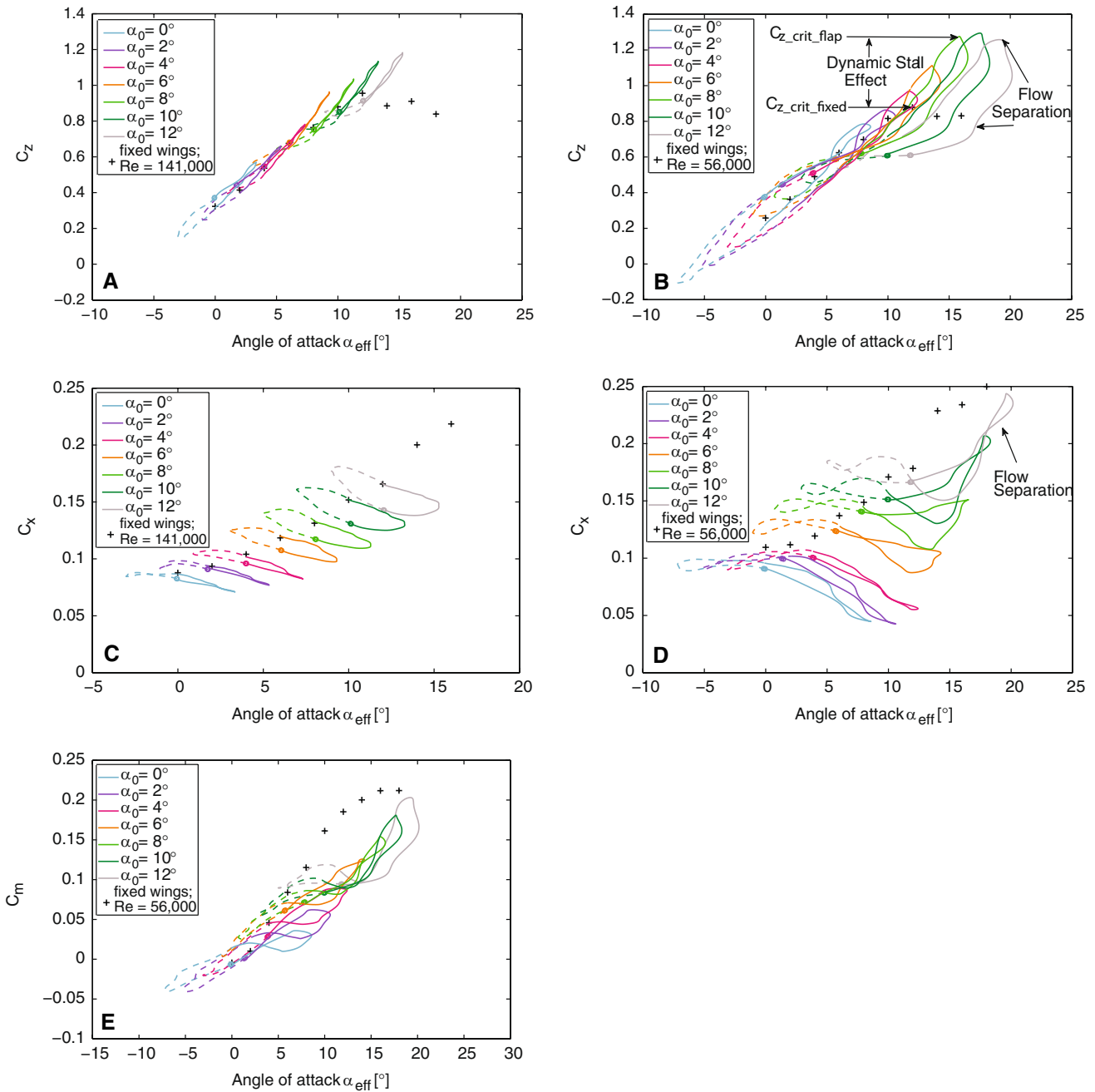


**Fig. 9** Force coefficient versus effective angle of attack ( $\alpha_{eff}$ ) at different static angle of attacks ( $\alpha_0$ ). **a**  $C_z$  for  $k = 0.04$  ( $f = 1.28$  Hz,  $Re = 141,000$ ). **b**  $C_z$  for  $k = 0.10$  ( $f = 1.28$  Hz,  $Re = 56,000$ ). The flapping wing results show the following unsteady effects: the critical vertical force coefficient ( $C_{z\_crit}$ ) for flapping wings is distinct higher than for fixed wings (indicating dynamic stall); different  $C_z$  values at identical  $\alpha_{eff}$  (indicating aerodynamic phase lag) and a rapid drop in  $C_z$  at high  $\alpha_{eff}$  (indicating flow separation) with long delays in

reattachment (hysteresis). **c**  $C_x$  for  $k = 0.04$  ( $f = 1.28$  Hz,  $Re = 141,000$ ). **d**  $C_x$  for  $k = 0.10$  ( $f = 1.28$  Hz,  $Re = 56,000$ ). Flow separation indicated by the sudden increase of  $C_x$  at  $\alpha_0 \geq 6^\circ$ . **d** Pitching moment coefficient ( $C_m$ ) versus effective angle of attack ( $\alpha_{eff}$ ) at different static angle of attacks ( $\alpha_0$ ) for  $k = 0.10$  ( $f = 1.28$  Hz,  $Re = 56,000$ ). Upstroke (dashed line); Downstroke (continuous line); lower reversal point (circle)

(Fig. 12a, b). In agreement to the quasi-steady assumption the highest lift was generated during the downstroke whereas the lowest lift was produced during the upstroke. At the reversal points the distribution was quite similar to

one another in case of a relatively low reduced frequency (Fig. 12a). However, there was a location shift in the onset of the circulation due to the asymmetrical amplitude of the flapping motion. At a considerably higher  $k$  (Fig. 12b) the

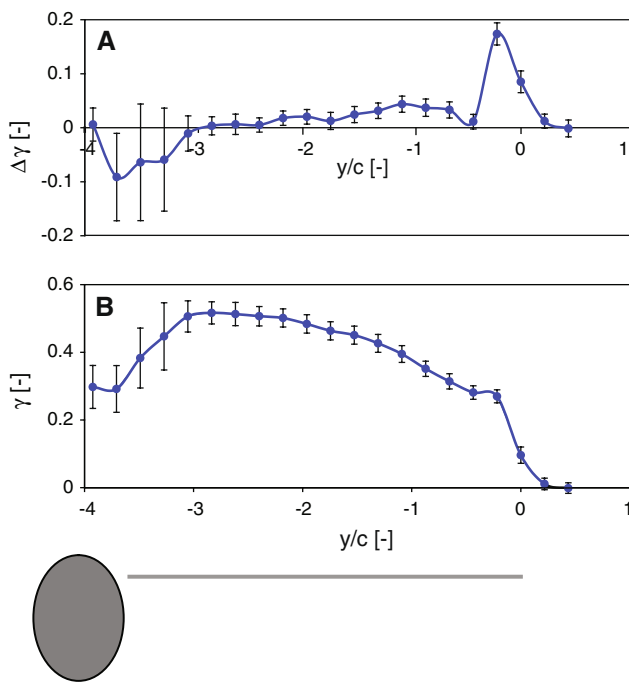


**Fig. 10** **a** Normalized circulation ( $\Delta\gamma$ ) and **b** distribution of the normalized circulation ( $\gamma$ ) over the span ( $y/c$ ) in the wake of the model with fixed wings (tip-vortex plane) at  $\alpha_0 = 8^\circ$  for  $Re = 113,000$ , averaged over 500 image pairs

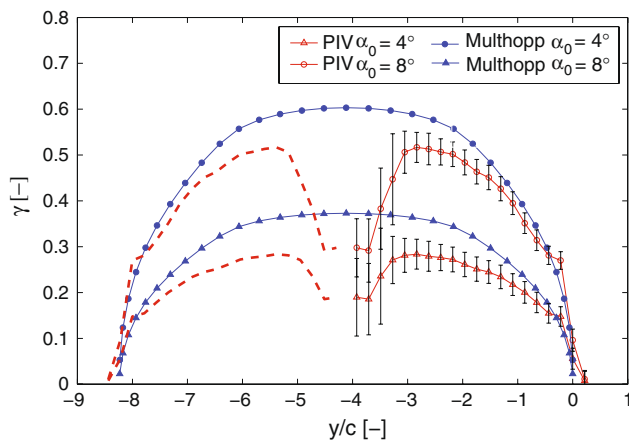


**Fig. 11** Distribution of normalized circulation ( $\gamma$ ) over the span ( $y/c$ ) in the wake of the model with fixed wings at  $\alpha_0 = 4^\circ$  and  $\alpha_0 = 8^\circ$  in comparison with calculated values (based on Multhopp) at  $Re = 113,000$ , averaged over 500 image pairs

aerodynamic phase lag caused a distinct difference in the distribution at the reversal points. While at a low reduced frequency ( $k = 0.05$ ) positive lift was generated over the entire wing-beat cycle, negative lift was generated in the phase close to the horizontal position during the upstroke at high reduced frequencies ( $k = 0.16$ ). A closer view at the change in the distribution at high  $k$  over the downstroke with elimination of the shift in the onset of the circulation

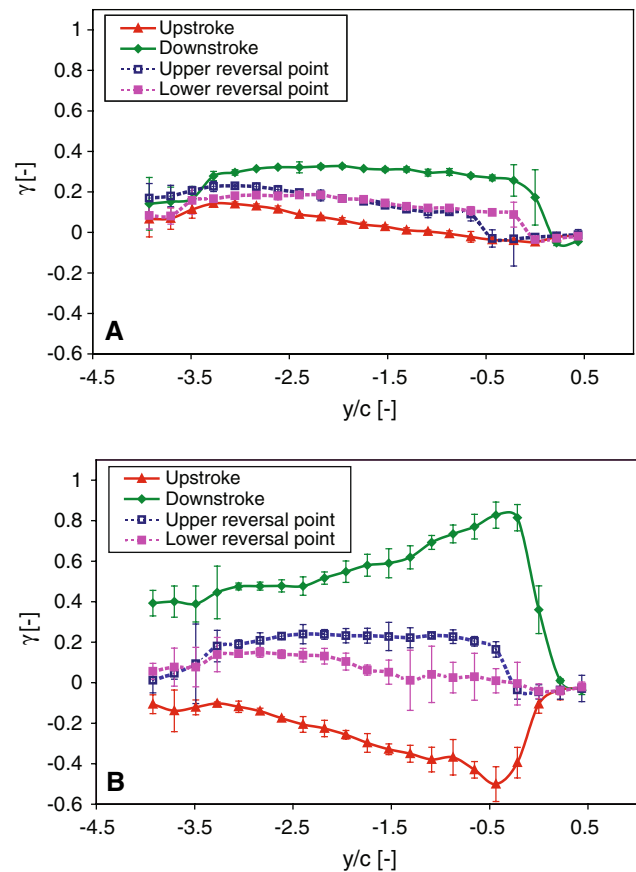


**Fig. 12** Distribution of normalized circulation ( $\gamma$ ) over the span ( $y/c$ ) in the wake of the model (tip-vortex plane) at the upper and lower reversal points as well as for the instant when the wing pass through the horizontal position during the upstroke and downstroke: **a** at  $k = 0.05$  ( $f = 1.28$  Hz,  $Re = 113,000$ ,  $\alpha_0 = 4^\circ$ ); **b** at  $k = 0.16$  ( $f = 2.02$  Hz,  $Re = 56,000$ ,  $\alpha_0 = 4^\circ$ )

due to wing motion showed that the peak in circulation shifted from the tip towards the root (Fig. 13). This is a clear indication of flow separation which then proceeded from the tip to the root. The flow separation during the downstroke also explains the large difference between the circulation distribution at the upper and lower reversal points compared to the results at lower  $k$ .

### 3.3 Comparison of balance and PIV results (Tip vortex plane)

The comparison between the  $C_L$  and  $C_z$  values showed a constant offset in the coefficients between the balance and PIV results (Fig. 14a–c). The offset was calculated by using unconstrained nonlinear optimization to determinate the optimal match of the PIV and balance results at different  $Re$ ,  $k$  and  $\alpha_0$ ; resulting in an average offset value of  $0.29 \pm 0.019$ . To permit a comparison of the relative changes during the wing beat cycle the minimum on the

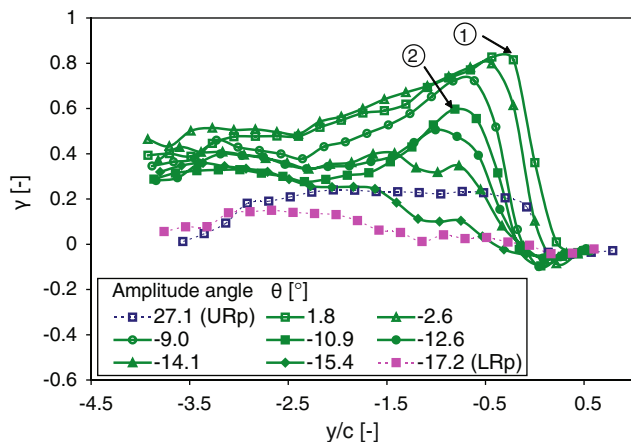


**Fig. 13** Distribution of normalized circulation ( $\gamma$ ) over the span ( $y'/c$ ) in the wake of the model for part of the downstroke at  $k = 0.16$  ( $f = 2.02$  Hz,  $Re = 56,000$ ,  $\alpha_0 = 4^\circ$ , tip-vortex plane, wing-fixed coordinate system  $y'$ , *URp* upper reversal point, *LRp* lower reversal point)

vertical scale was shifted while the scaling of both axes remained the same. The change in the circulation during the wing beat cycle calculated from the PIV results complied well with the balance results. The maximum change in circulation over the wing beat cycle was used to define the discrepancy between PIV and balance results, comparing the difference between maximum and minimum of  $C_z$  and  $C_L$  within the wing beat cycle at different  $k$ . At  $k = 0.05$  and  $k = 0.08$  discrepancy was 3.29 and 3.48% referring to the balance results. At  $k = 0.16$  the discrepancy was much higher (26.6%), due to the high differences during the second phase of the downstroke, when  $\alpha_{\text{eff}}$  is high above  $\alpha_{\text{crit}}$  and unsteady effects and flow separation occurred. The reason for the necessary offset has not been resolved.

### 3.4 Comparison of PIV results (Tip and transverse vortex plane)

The comparison of the change of circulation calculated from the different planes showed a similar magnitude and shape (Fig. 15a). The agreement depends on the Reynolds number and the reduced frequency. High Reynolds numbers and low reduced frequency measurements showed a better agreement than at highly unsteady conditions. However, the turbulence and influence of the pressure equalization due to the wing/body gap increased with increasing Reynolds number and reduced frequency in the area close to the body (Fig. 15b). The fluctuation and turbulence level in the area near the body is significantly higher than in the distal regions, which is in agreement with the high standard deviation of the circulation in this area for fixed wings (Fig. 10). In addition, the change in

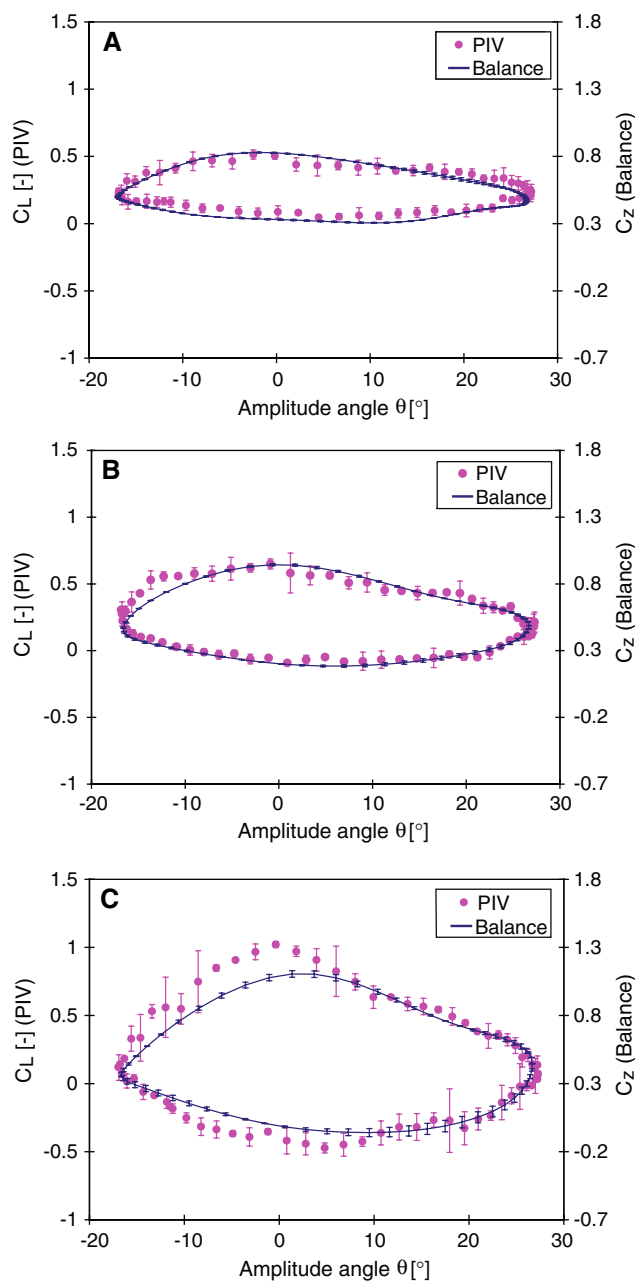


**Fig. 14** Comparison of lift coefficient ( $C_L$ ), calculated from the visualized circulation, and vertical force coefficient ( $C_z$ ) measured with the balance over the wing beat cycle at different  $k$ : **a** at  $k = 0.05$  ( $f = 1.28$  Hz,  $Re = 113,000$ ,  $\alpha_0 = 4^\circ$ ); **b** at  $k = 0.08$  ( $f = 2.02$  Hz,  $Re = 113,000$ ,  $\alpha_0 = 4^\circ$ ); **c** at  $k = 0.16$  ( $f = 2.02$  Hz,  $Re = 56,000$ ,  $\alpha_0 = 4^\circ$ ). The PIV coefficients are averaged over 25 image pairs, the balance results were displayed on a second  $y$  axis due to the constant offset of 0.3 in the force coefficients, while the scaling was the same, the standard deviation is included for both PIV and balance measurements (displayed only for every third value for the balance)

circulation at this position was asymmetric and the positive and negative circulation was not equalized at the end of the wing-beat cycle, showing the three-dimensional nature of the wake.

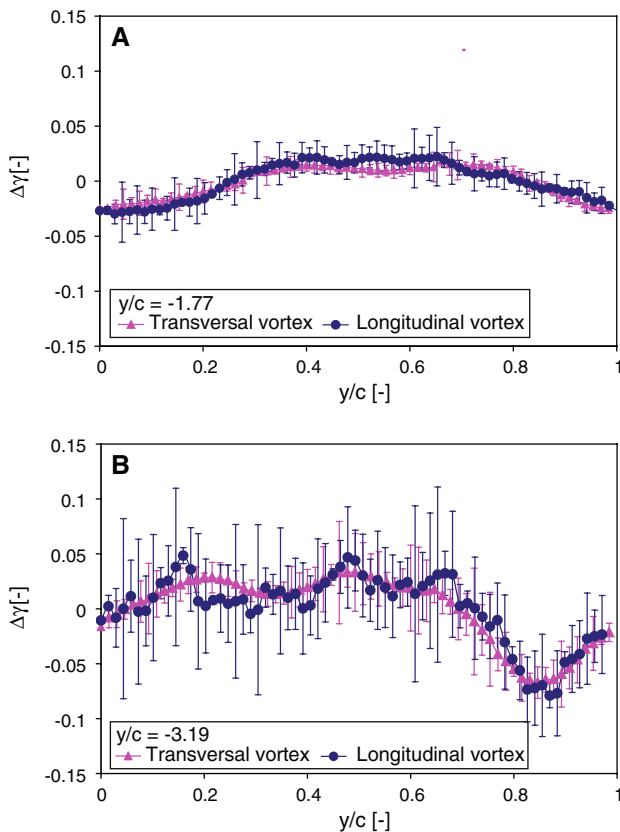


**Fig. 15** Change in circulation ( $\Delta\gamma$ ) over the wing-beat cycle calculated from the tip-vortex plane (longitudinal vortex) perpendicular to the flow stream and the transverse-vortex plane (transversal vortex) parallel to the flow stream at  $k = 0.08$  ( $f = 2.02$  Hz,  $Re = 113,000$ ,  $\alpha_0 = 4^\circ$ ). **a** At a distal wingspan position ( $y/c = -1.77$ ), **b** at a proximal wingspan position ( $y/c = -3.19$ )

## 4 Discussion

### 4.1 Direct force measurement

The results of the fixed wings measurements with the balance, which were used for reference purposes, showed good agreement with the results of the 2D Wortmann profile (Althaus 1981) after applying lifting line theory to account for the finite wingspan.

Consideration of inertial forces and the added mass effect, revealed that the vertical force generation over the upstroke was considerably lower than during the downstroke, agreeing with the expectation based on quasi-steady assumptions. At moderate  $k$  and  $Re$  the inertial forces were slightly lower than the aerodynamic forces and the added mass effect was about 10%, agreeing in magnitude with calculations based on a sinusoidal movement.

Lift was produced mainly by the wings since the body itself generated very little lift ( $C_{L\_Body} \approx 0.02$ – $0.03$ ). In contrast to the lift, the body was the main source of drag ( $C_{D\_Body} \approx 0.08$ ).

Increasing the static angle of attack  $\alpha_0$  for flapping wings resulted in a change in  $C_z$ , similar to the that of an oscillating airfoil described by McCroskey (1981). According to McCroskey the high  $\alpha_{eff}$  in combination with the wing movement induce a high fluctuating pressure field which is related to the delayed stall phenomena.

Provided that the flapping frequency, angle of attack and amplitude is high enough, a well-structured leading edge vortex (LEV) is formed. As long as the LEV remains stable it leads to a high lift coefficient. However, as soon as the vortex is shed at the trailing edge, stall sets in and the reattachment of the flow with decreasing  $\alpha_{eff}$  is delayed, clearly expressed by a large hysteresis loop. This hysteresis loop was clearly seen in the flapping wing results, when  $\alpha_{eff}$  was high enough due to high  $k$  and high  $\alpha_0$ . At the same time the onset of stall is related to an abrupt increase in drag and pitching moment, likewise clearly visible in the balance results. Contrary to insect flight, where additional lift generation due to unsteady effects, such as wake capture, rotational lift and delayed stall, has been substantially documented during the last decade (Bomphrey et al. 2005; Dickinson et al. 1999; Lehmann 2004), Vertebrate flight has often been treated as quasi-steady, and only recently has it been questioned whether or not the delayed stall effect also plays a role in bird and bat flight. Investigations on small birds like hummingbirds and swifts are in progress. A leading-edge vortex was found so far on static swift wings (Videler et al. 2004), which are characterized through sharp leading edges and high swept-back configurations (delta wing like), both features supporting the development of a leading edge vortex. In the case of hummingbirds, whose flight style shows similarities to large insect flight, a dynamically scaled flapping flat plate ( $Re \sim 4,000$ ) clearly showed the development of a LEV during mid upstroke and downstroke but could not be visualized on the bird itself (Tobalske et al. 2008). The occurrence of LEVs in bat flight ( $<10$  g,  $U_\infty = 1$  m/s) was recently discovered (Muijres et al. 2008). The present observations of high vertical force coefficients of the flapping goose model at higher  $\alpha_{eff}$  leads to the assumption that there were phases in the wing beat cycle when a leading edge vortex developed, in spite of round leading edges and the lack of similarity to insect flight. However, due to the 3D wing movement, the balance results gave no information about the stability of the LEV. According to Ellington (1999) and Liu et al. (1998) the lateral flow, as a result of the flapping movement, is responsible for the stabilization of the leading edge vortex. However, Birch and Dickinson (Birch et al. 2004) claimed that the importance of the lateral flow depends on the Reynolds number. To what extent the lateral flow played a role in the present case is unknown; a lateral flow component could not be visualized behind the wing and probably requires

measurements on the surface of the wing itself. Measurements on the wing could also confirm the assumption that the delayed stall effect was responsible for the enhanced lift generation, by detecting the LEV. Of course measurements on a flapping wing introduce other, rather difficult obstacles to the experimental configuration.

#### 4.2 Flow visualization perpendicular to the flow stream (tip-vortex plane)

One of the goals of the investigation was to obtain an answer to the question of whether 2D PIV measurements can be used to obtain the forces on flapping wings, based on the Helmholtz vorticity laws and lifting line theory. One has to be aware of the limitation of the 2D measurement procedure. The aerodynamic forces on an object can be obtained by using the control-volume approach and applying the momentum equation and taking into account the total surface forces over the entire control volume. However, even in steady locomotion such as in cruising flight, the propulsion area and actually the whole body of the animal is subjected to a periodic acceleration and deceleration. These unsteady flow conditions around the body lead to the problem that an exact determination of aerodynamic or hydrodynamic forces requires measurement of the net flow of momentum out of the control volume surface as well as the time rate of change due to the unsteady fluctuations inside the control volume itself (Dabiri 2005). So, to obtain the actual forces, the whole volume of the flow field has to be recorded by time-resolved tomographic PIV (Arroyo and Hinsch 2008), to fulfill the requirements of the momentum equation, which up to now has only been possible for very limited volumes. 2D measurements by nature can therefore only provide an approximation of the actual forces.

Measurements downstream of the trailing edge require the consideration of the time delay between the visualization and the events on the wing itself. However, even if the comparison of the change in circulation obtained by PIV and balance measurements confirm the usability of the free-stream velocity to relate the visualization in the observation plane with the wing position, one should keep in mind that due to the spanwise dependency of the roll up process, the vorticity information contained in the observation plane at any particular instant originates at different times across the wingspan.

Nevertheless, the distribution of the circulation estimated from the visualization in the tip-vortex plane 2.2c behind the wings agreed well with the distribution based on simple quasi-steady assumptions, except for the near-body region. Negative circulation was generated close to the body due to the pressure equalization in the gap between body and wing and high turbulence and laser light sheet

reflections led to high standard deviations of the velocity measurements. The total circulation based on the Multhopp calculation was significant higher than the PIV based results due to the poor modeling of the near-body region.

The circulation distribution over the wing beat cycle exhibited, in addition to an increasing aerodynamic phase lag, an increasing difference between upstroke and downstroke with increasing  $k$ . At higher  $k$  negative circulation was observed at the distal areas of the wing during the upstroke. Flow separation can be observed over the downstroke, indicated by the change in location of the peak in circulation towards the body, which also provides the explanation for the increasing difference in circulation at the two reversal points.

#### 4.3 Comparison of balance and PIV results (tip vortex plane)

PIV and balance results showed good agreement in the change of circulation over the wing beat cycle. However, the degree of accuracy was related to the flow conditions and decreases with increasing  $k$ . This can be explained partly due to the comparison of  $C_L$  and  $C_z$ , while at low  $k$  ( $k = 0.05$ ) the difference between the two coefficients was estimated to reach a maximum of about 1.6% of  $C_L$ : there is a significant increase in the difference with increasing  $k$  ( $k = 0.16$ , 4.2%;  $k = 0.25$ , 8.6%). However, the main source of the difference is the increasing influence of flow separation and unsteady effects, as is evident from the agreement at high  $k$  in wing beat phases of low  $\alpha_{\text{eff}}$ , but less accuracy in phases of extraordinary high  $\alpha_{\text{eff}}$ .

Independent of  $Re$ ,  $k$  and  $\alpha_0$  there was constant offset of  $0.29 \pm 0.019$  in the absolute value of the lift and vertical force coefficient of the PIV and balance. There are two possible explanations for this offset. One is an error in the measurements technique itself either in the balance or PIV measurements. Another possibility was that significant information was missing in the force calculations based on the flow visualization due to the limitation to 2D measurements and the downstream position of the observation area.

To eliminate any mistake in the direct force measurements, additional fixed wing measurements were performed using an external balance and different software. Apart from the results at  $Re = 28,000$ , the discrepancy between external and internal balance results was lower than 5%. The discrepancy was most likely the result of the interference between model and support and due to the external balance range of  $\pm 6,000$  N, which limited the resolution. Furthermore the balance results at  $Re = 56,000$  matched the expected literature results of the Wortmann FX 60-126 profile at  $Re = 100,000$ .

A mistake in the PIV calculation was dismissed due to the fit in the change of circulation in the balance and PIV

results as well as with the results in the transverse vortex plane.

Important evidence was that the offset was constant for the non-dimensional coefficient therefore the offset of the force itself depended on the free stream velocity which made it unlikely to be an offset in the measurement equipment itself.

The observation area was considered as appropriately large to avoid the loss in circulation, especially because the vector fields showed that the circulation was located close to the wing tip. A loss of information caused by the slight change in orientation of the vortex with respect to the observation plane was considered; however, it was ruled out as an explanation because the offset did not change significantly for different static angles of attack.

The obstruction based on the frontal area was less the 0.4% and the distance to each wind tunnel wall  $> 0.8$  m, eliminating any influence of vortex wall interaction under consideration of the magnitude of the generated forces.

In the hummingbird related investigations of the flat plate robotic wing (Tobalske et al. 2008) the calculated force from the circulation of the tip vortex matched the measured forces within one chord length but showed only 50% of the measured forces at  $2c$ , which was explained by the instability of the shed vortices. However, any instability and dissipation should be influenced by the change in flow speed and should increase for low speed due to the constant distance between observation area and trailing edge.

Wake vortex added mass effects can lead to an underestimation of the necessary forces in swimming and flying using wake measurement (Dabiri 2005). However, while they represent an additional force that contributes to the necessary power input, vortex added mass effects went undiscovered for a long time because they cannot be noticed in the time averaged forces. Only recently, with increasing time resolved measurements, have they been examined more closely. However, the magnitude of the vortex added mass effect for these measurements can be assumed to be small and the offset is still present in the time averaged forces for balance and PIV results, therefore the vortex added mass effect does not provide a sufficient explanation for the difference in PIV and balance results.

Up to now none of these effects offered a satisfying explanation for the observed offset. While influences of dissipation, added mass and loss off information due to the limited 2D measurements certainly are a source of possible errors, the loss would be assumed to be much smaller than the observed 100%. Any explanation so far is in contradiction to the fact that while the absolute value differed of a constant value of 0.29 (independent of Reynolds number and reduced frequency) the relative change in circulation was in agreement with the results of the direct force measurements.

The body wing area was a source of high turbulence and the gap between wing and body, which was mechanically necessary, was an additional complication. The gap allowed a considerably pressure equalization between the upper and lower surfaces of the wing, as could be seen in the decline in circulation in the near-body region. In addition, the laser light reflections off the body made the flow measurements more difficult and increased the standard deviation of the velocity values in this region. The comparison between quasi-steady calculations (Multhopp) and experimentally acquired distributions supports the theory of a wing/body gap explanation due to the good agreement in circulation in the distal areas, but significantly different absolute values due to the negative circulation in proximal areas (Fig. 13). The Multhopp based calculation for the absolute force generated were in the range of the results from the direct force measurements, while the PIV results were considerably lower, which might be an additional indication that the difference is due to the drop in circulation in the near body area. However, there is no satisfying explanation to why this drop in circulation should not be reflected in the force measurements.

After careful consideration of possible fluid dynamic explanations as well as errors in the measurement techniques itself, the authors have yet to find a sufficient explanation for the extremely high value of the offset.

#### 4.4 Comparison of PIV results (Tip and transverse vortex plane)

The comparison of the change in circulation over the wing beat calculated from the two perpendicular planes (tip and transverse) showed very good agreement. Differences can be explained by the fact that the distribution in the wake differ from the distribution on the wing itself due to the roll-up process and a highly three-dimensional flow field. The turbulence and highly three-dimensional flow conditions close to the body caused significantly higher disturbances in the results of the transverse vortex plane than the tip vortex plane.

## 5 Conclusions

Wake PIV measurements in two planes perpendicular to each other (tip and transverse vortex plane) were performed in addition to direct force measurements with a three-component balance, with the goal to verify the appropriateness of quasi-steady assumptions in the range of bird flight and the qualification of simple 2D PIV measurements to obtain the generated forces on flapping wings.

The results of the direct force measurements were qualified to give good insight into the flow conditions on

the wings. Even if the measurements on flapping wings are difficult to perform and require certain assumptions and simplifications, unsteady effects and flow separation could clearly be recognized.

Typically the balance results showed a significantly higher vertical force coefficient for flapping wings compared to the maximum coefficient of the fixed-wing results. It is postulated that this was caused by the delayed stall effect, a phenomenon which occurs on plunging or pitching airfoils. This indicates that the flow around the wing cannot be simplified as a quasi-steady flow.

When flow separation occurs over large parts of the wing, the influence could be seen in a hysteresis loop in the vertical force coefficient and a sudden increase in horizontal force generation.

One should keep in mind that due to the movement around a shoulder joint, the flow conditions are entirely three dimensional and the flow conditions change along the span. While the flow can be still attached at proximal wing positions, unsteady effects such as delayed stall, can be developed at distal positions and flow separation occurs in the outward direction. The results of the balance showed only the net result of different conditions along the wingspan and different effects as flow separation and delayed stall could even be compensating.

It was assumed that the measurements in the tip vortex plane provide the absolute value of the circulation on the wing itself as well as the change in circulation and the distribution along the span over the wing beat cycle. While the absolute value of the circulation was not reliable, the change in circulation over the wing beat cycle agreed well with the balance results and with the calculations from the transverse vortex plane measurements. The agreement is typically higher at high Reynolds numbers and low reduced frequencies and tended to decline under highly unsteady conditions and highly three-dimensional flow conditions.

The measurements in the tip vortex plane and the transverse vortex plane at different positions along the wingspan provided insight into the distribution of the circulation. However, measurements close to the body were more difficult to perform. The change in distribution over the wing beat cycle obtained through the measurements in the tip vortex plane showed clear indications of flow separation, but further measurements on the wing itself would be necessary to show the separation and assumed delayed stall effect conclusively. The agreement in the distribution of the circulation obtained by wake measurements with the circulation distribution on the wing itself depends on the proximity of the measurements to the wing as well as the flow velocity, reduced frequency and the spanwise position. Nevertheless, with due consideration of the factors influencing the PIV accuracy, this method can be used to

provide useful insights into the flow conditions on a model with flapping wings.

## References

- Althaus D (1981) Wortmann, F.X.: Stuttgarter Profilkatalog Braunschweig
- Arroyo M, Hinsch K (2008) Recent developments of PIV towards 3D measurements. In: Particle image velocimetry, vol 112. Springer, Berlin, pp 127–154
- Birch JM, Dickson WB, Dickinson MH (2004) Force production and flow structure of the leading edge vortex on flapping wings at high and low Reynolds numbers. *J Exp Biol* 207:1063–1072
- Bomphrey RJ, Lawson NJ, Harding NJ, Taylor GK, Thomas ALR (2005) The aerodynamics of *Manduca sexta*: digital particle image velocimetry analysis of the leading-edge vortex. *J Exp Biol* 208:1079–1094
- Cloupeau M, Devillers JF, Devezeaux D (1979) Direct measurements of instantaneous lift in Desert Locust; comparison with Jensen's experiments on detached wings. *J Exp Biol* 80:1–15
- Dabiri JO (2005) On the estimation of swimming and flying forces from wake measurements. *J Exp Biol* 208:3519–3532
- Dickinson MH, Gotz KG (1996) The wake dynamics and flight forces of the fruit fly *Drosophila melanogaster*. *J Exp Biol* 199:2085–2104
- Dickinson MH, Lehmann F, Sane SP (1999) Wing rotation and the aerodynamic basis of insect flight. *Science* 284:1954–1960
- Dickson WB, Dickinson MH (2004) The effect of advance ratio on the aerodynamics of revolving wings. *J Exp Biol* 207:4269–4281
- Drucker EG, Lauder GV (1999) Locomotor forces on a swimming fish: three-dimensional vortex wake dynamics quantified using digital particle image velocimetry. *J Exp Biol* 202:2393–2412
- Ellington CP (1999) The novel aerodynamics of insect flight: applications to micro-air vehicles. *J Exp Biol* 202:3439–3448
- Hedrick TL, Usherwood JR, Biewener AA (2004) Wing inertia and whole-body acceleration: an analysis of instantaneous aerodynamic force production in cockatiels (*Nymphicus hollandicus*) flying across a range of speeds. *J Exp Biol* 207:1689–1702
- Hubel T (2006) Untersuchungen zur instationären Aerodynamik an einem vogelähnlichen Flügelschlagmodell In: Department of Biology. PhD, Darmstadt University of Technology, Darmstadt, p 194
- Lehmann F-O (2004) The mechanisms of lift enhancement in insect flight. *Naturwissenschaften* 91:101–122
- Liu H, Ellington CP, Kawachi K, Van Den Berg C, Willmott AP (1998) A computational fluid dynamic study of hawkmoth hovering. *J Exp Biol* 201:461–477
- Maybury WJ, Rayner JMV (2001) The avian tail reduces body parasite drag by controlling flow separation and vortex shedding. *Proc R Soc B Biol Sci* 268:1405–1410
- McCroskey WJ (1981) The phenomenon of dynamic stall. NASA TM-81264
- Mueller TJ (2001) Fixed and flapping wing aerodynamics for micro air vehicle applications. Progress in astronautics and aeronautics, vol 195, AIAA, New York
- Muijres FT, Johansson LC, Barfield R, Wolf M, Spedding GR, Hedenstrom A (2008) Leading-edge vortex improves lift in slow-flying bats. *Science* 319:1250–1253
- Multhopp H (1938) Die Berechnung der Auftriebsverteilung von Tragflügeln. *Luftfahrt-Forschung* 4:153–169
- Rayner JMV, Gordon R (1998) Visualization and modelling of the wakes of flying birds, vol 13. Gustav Fischer Verlag, Jena



- Sane SP (2003) The aerodynamics of insect flight. *J Exp Biol* 206:4191–4208
- Spedding GR (1987a) The wake of a Kestrel (*Falco tinnunculus*) in flapping flight. *J Exp Biol* 127:59–78
- Spedding GR (1987b) The wake of a Kestrel (*Falco tinnunculus*) in gliding flight. *J Exp Biol* 127:45–57
- Spedding GR (1986) The wake of a Jackdaw (*Corvus monedula*) in slow flight. *J Exp Biol* 125:287–307
- Spedding GR, Hedenström A, Rosén M (2003a) Quantitative studies of the wakes of freely flying birds in a low-turbulence wind tunnel. *Exp Fluids* 34:291–303
- Spedding GR, Rayner JMV, Pennycuik CJ (1984) Momentum and energy in the wake of a pigeon (*Columba livia*) in slow flight. *J Exp Biol* 111:81–102
- Spedding GR, Rosen M, Hedenstrom A (2003b) A family of vortex wakes generated by a thrush nightingale in free flight in a wind tunnel over its entire natural range of flight speeds. *J Exp Biol* 206:2313–2344
- Thomas ALR, Taylor GK, Srygley RB, Nudds RL, Bomphrey RJ (2004) Dragonfly flight: free-flight and tethered flow visualizations reveal a diverse array of unsteady lift-generating mechanisms, controlled primarily via angle of attack. *J Exp Biol* 207:4299–4323
- Tobalske BW, Warrick DR, Dickson WB, Altshuler DA, Dickinson MH (2008) Hovering aerodynamics in hummingbirds: comparing a dynamically-scaled robot with live birds. In: Society for Integrative and Comparative Biology, 2008 Annual Meeting, San Antonio
- Usherwood JR, Hedrick TL, Biewener AA (2003) The aerodynamics of avian take-off from direct pressure measurements in Canada geese (*Branta canadensis*). *J Exp Biol* 206:4051–4056
- Usherwood JR, Hedrick TL, McGowan CP, Biewener AA (2005) Dynamic pressure maps for wings and tails of pigeons in slow, flapping flight, and their energetic implications. *J Exp Biol* 208:355–369
- Videler J, Stamhuis E, Povel D (2004) Leading-edge vortex lifts swifts. *Science* 306:1960–1962
- Walker JA (2002) Rotational lift: something different or more of the same? *J Exp Biol* 205:3783–3792
- Warrick DR, Tobalske BW, Powers DR (2005) Aerodynamics of the hovering hummingbird. *Nature* 435:1094–1097
- Webb PW (1975) Hydrodynamics and energetics of fish propulsion. *Bull Fish Res Bd Can* 190:1–158
- Wilkin PJ (1990) The instantaneous force on a desert locust, *Schistocerca gregaria* (Orthoptera: Acrididae), flying in a wind tunnel. *J Kansas Ent Soc* 63:316–328
- Wilkin PJ (1991) Instantaneous aerodynamic forces developed by an Indian Moon Moth, *Actias selene*, in near hovering flight. *Physiol Zool* 64:193–211
- Wilkin PJ, Williams MH (1993) Comparison of the instantaneous aerodynamic forces on a sphingid moth with those predicted by quasi-steady aerodynamic theory. *Physiol Zool* 66:1015–1044
- Willmott AP, Ellington CP, Thomas ALR (1997) Flow visualization and unsteady aerodynamics in the flight of the hawkmoth, *Manduca sexta*. *Philos Trans Biol Sci* 352:303–316
- Zarnack W (1969) Kinematik der Flügelbewegungen bei *Locusta migratoria* L. Math-Nat-Fak. Dissertation, Munich: Universitaet Muenchen